ADVANCED MATERIALS TECHNOLOGIES
www.advmattechnol.de

Construction of PTFE/Nafion Composite Membrane with Ultrathin Graphene Oxide Layer for Durable Fuel Cells

Eunho Choi, Hojin Kang, Yeonghwan Jang, Ji Hoon Kim, Ho Seon Ahn, Sang Moon Kim, and Segeun Jang**

The long-term operation of polymer electrolyte membrane fuel cells (PEMFCs) relies heavily on the durability of the perfluorinated sulfonic acid (PFSA, e.g., Nafion) membrane against chemical and mechanical degradation. To mitigate mechanical degradation, the introduction of a reinforcing matrix, such as a porous PTFE sheet, is employed. However, completely impregnating the PFSA ionomer into the PTFE sheet through the conventional blade-coating method using a highly viscous ionomer solution proves challenging. This limitation results in decreased mechanical and proton transport properties. To reduce proton transport resistance, thinner membrane thickness is desirable, although it increases the amount of gas crossover, which generates radicals and accelerates the chemical degradation of the membrane. In this study, a spraying process utilizing a low viscous-solvent-rich ionomer solution is experimentally optimized to construct a well-impregnated PTFE/Nafion membrane and analyzed using a simple theoretical droplet-spreading model. Furthermore, an ultrathin graphene oxide (GO) layer is introduced during the membrane fabrication process with the same spraying technique for reducing gas crossover while minimizing performance loss. The membrane electrode assembly (MEA) with the prepared PTFE/Nafion membrane-incorporated ultrathin GO layer shows significantly greater durability and initial performance compared to the conventional MEA.

1. Introduction

Polymer electrolyte membrane fuel cells (PEMFCs) have emerged as a promising and sustainable technology for stationary and automotive applications.[1] To meet the growing demand for requirements of extended lifetime in large-scale stationary applications (≈40 000 h) and public transportation such as taxis or buses (>20 000 h),[2] enhancing both the chemical and mechanical durability of the membrane is necessary.[3] The most commonly used material in PEMFCs is the perfluorinated sulfonic acid (PFSA) membrane, representatively Nafion (Dupont Co.), due to its high proton conductivity as well as suitable chemical and mechanical stabilities.[4,5] However, the high cost of PFSA must be considered when commercializing PEMFCs for the aforementioned applications, as it takes up to 12% of the total fuel cell stack cost when considering 100 000 systems per year.[6] Reducing the membrane thickness can lead to cost reduction and minimize resistance by shortening the proton transport route; however, it can sacrifice the membrane's mechanical durability and accelerate the reactant gas crossover through the membrane, which in turn promotes radical generation-induced chemical degradation.

Several studies have been conducted to develop polytetrafluoroethylene (PTFE)/Nafion (P/N) reinforced composite membranes (RCMs) using porous PTFE sheets to improve their mechanical properties.[7,8] This is because PTFE has high thermal resistance as well as excellent mechanical and chemical endurance, and the backbone of the Nafion is composed of PTFE.[9,10] This approach has enabled the fabrication of thin membranes with minimal usage of PFSA ionomer, and with this advantage, commercial products such as GORE-SELECT have been represented as a successful case.[11,12] However, incomplete impregnation of the ionomer into the PTFE sheet through the conventional blade-coating method using a highly viscous PFSA solution results in interfacial incompatibility between hydrophilic ionomers and hydrophobic PTFE fibers.[13–15] Therefore, it reduces proton transport and mechanical durability and increases high-reactant gas crossover. Notably, thinner membranes exacerbate the gas crossover issue and accelerate radical (e.g., HO•, HOO•) generation through the Fentons' reaction of chemical species of dissolved metal ions (e.g., Fe^{2+}) and H_2O_2.[16,17] These radicals are supplied from the corrosion of the bipolar plate (or humidifier) and the direct chemical reaction of H_2 and O_2 on the catalyst, respectively.[18] These reactive oxygen radicals attack the membrane and electrode, resulting in catastrophic failure characterized by membrane thinning,

E. Choi, H. Kang, Y. Jang, S. Jang
School of Mechanical Engineering
Kookmin University
Seoul 02707, Republic of Korea
E-mail: sjang@kookmin.ac.kr
J. H. Kim, H. S. Ahn, S. M. Kim
Department of Mechanical Engineering
Incheon National University
Incheon 22012, Republic of Korea
E-mail: ksm7852@inu.ac.kr

The ORCID identification number(s) for the author(s) of this article can be found under https://doi.org/10.1002/admt.202301191

DOI: 10.1002/admt.202301191

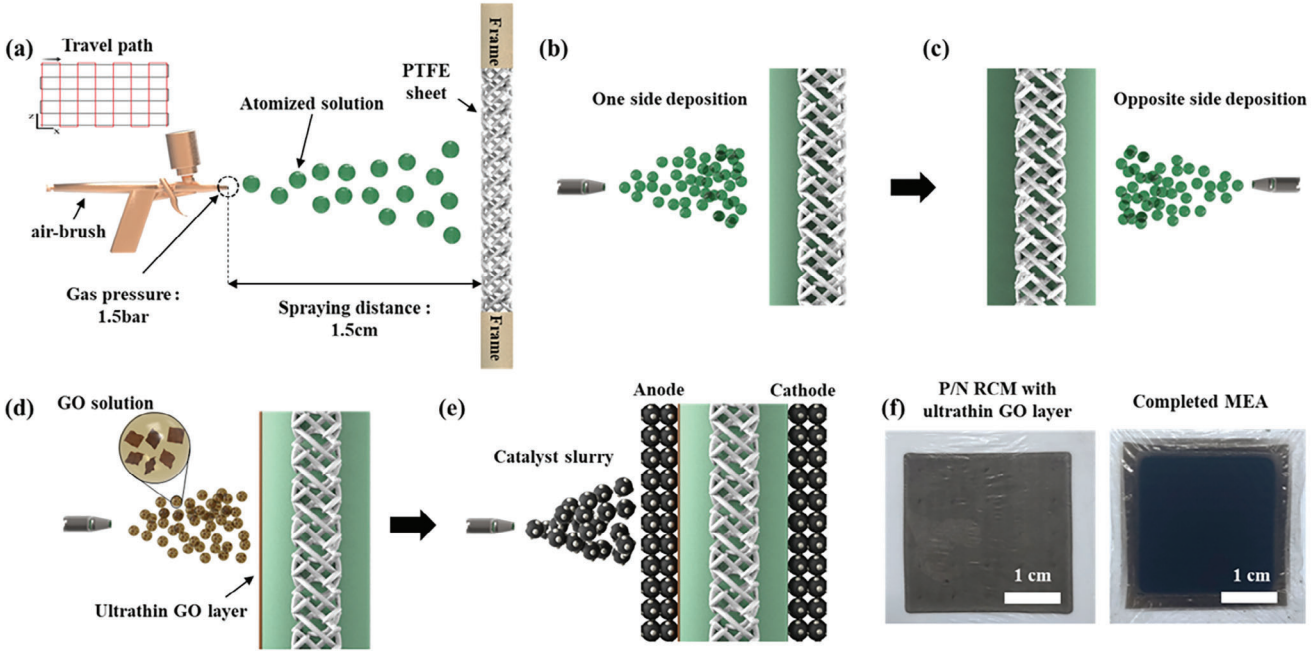

Figure 1. Schematics of the fabrication process of P/N RCM with an ultrathin GO layer and MEA by the spraying method. a) Spraying deposition system. b,c) Consecutive spraying of an ionomer solution to a porous PTFE sheet on both the anode and cathode sides. d) Spraying a GO solution on the anode side of P/N RCM. e) Fabrication of MEA by deposition of a catalyst ink to the prepared membrane. f) Digital camera images of P/N RCM with an ultrathin GO layer (left) and the constructed MEA (right).

pinhole generation, ionomer degradation, and the oxidized carbon support of the catalyst.[4,19,20]

To address the issues associated with radical attack-induced chemical degradation, the incorporation of radical scavengers such as CeO_2 within the membrane and electrode has been widely adopted as an effective strategy.[21–23] Although the modified membrane with CeO_2 showed dramatically improved chemical stability during long-term operation, inevitable proton conductivity loss has been observed because non-proton conducting CeO_2 nanoparticles tend to be agglomerated inside the membrane and Ce^{3+}/ Ce^{4+} ion substitutes the proton at the sulfonic acid group.[24–26] The mobility of cerium ions during cell operation can reduce scavenging efficacy and cell performance.[27,28] As an another approach to improving the chemical durability of the membrane, the use of 2D materials such as graphene oxide (GO)[29–32] and hexagonal boron nitride (h-BN)[33] has been reported as a viable physical solution for introducing a gas barrier within the membrane. When introducing a gas barrier using 2D materials, forming a thin-stacked layered structure is required to ensure proton conductivity while effectively preventing the crossover of gas molecules. However, conventional blading-coating and solution-casting techniques are not applicable. Lee et al.[33] proposed a direct spin-coating method with 2D hBN on the commercial Nafion membrane surface and observed significantly reduced gas crossover and improved chemical durability during an open circuit voltage (OCV) holding accelerated stress test. Although spin coating enables the deposition of ultrathin layers on the membrane surface, it is challenging to achieve a scale-up process and uniform coating due to the solution droplet-induced local membrane swelling.

In this study, a spraying method for P/N RCM construction is presented. To determine the optimized conditions for the effective impregnation of ionomers into a porous PTFE sheet, different flow rates of a low viscous-solvent-rich ionomer solution are investigated experimentally and theoretically. To secure the gas barrier property of thin P/N RCM (≈10 μm), an additional ultrathin GO-stacked layer (≈150 nm) was sprayed at the membrane's anode side during the membrane fabrication process by applying the same spraying method. Comparisons of different GO loading amounts, as well as spatial arrangement of GO powders as layered or dispersed forms in the membrane, were made. Compared to the MEA with commercial NRE 211 membrane (≈25 μm), the MEA with a modified P/N RCM containing an ultrathin GO layer showed improved initial performance, thanks to its thin-thickness and well-impregnation characteristic, as well as enhanced chemical and mechanical durability due to the mechanically reinforcing effect of PTFE and alleviated radical generation by using GO as a gas-crossover barrier.

2. Results and Discusion

2.1. Fabrication of P/N RCM-UG

Figure 1a shows schematics of the spraying system used to construct P/N RCM with an ultrathin GO layer (P/N RCM-UG) and MEA. First, to secure uniform deposition characteristics, a serpentine-like spray-travel path was applied. At the end of the path, the serpentine pattern was rotated by 90°, and the center position of the nozzle was shifted by halfwidth of spray-spot size (≈1 mm). For the spraying system, a commonly used airbrush was employed, and the pressure and distance of the nozzle to the

substrate were fixed at 1.5 bar and 1.5 cm, and the flow rate with spraying ionomer solutions was set to key factor determining the degree of ionomer impregnation into a porous PTFE sheet. In Figure 1b,c, the ionomer solution was sprayed to both sides of the PTFE sheet to fully impregnate the ionomer solution into the sheet. A low-viscous ionomer solution comprised a weight ratio of IPA: 1-propanol: DI water: ionomer = 80:10:9:1. As shown in Figure S1 (Supporting Information), while the DI water has a high contact angle of 142.3° on the hydrophobic porous PTFE sheet, the IPA has a small contact angle of 24.8°. This means that wetting the PTFE with IPA, which has low surface tension, can help the ionomer solution impregnate inside the nanoporous PTFE through capillary action. However, due to the high evaporation pressure of the IPA-rich solution, achieving full impregnation of the ionomer on the opposite side of the PTFE sheet becomes challenging. Additionally, even if the ionomer reaches the end, adequately covering the exposed opposite side of the PTFE sheet surface poses a significant challenge (Figure S2, Supporting Information), which severely impedes proton transfer to the interface of the membrane/electrode where the catalytic reaction occurs dominantly. Therefore, the ionomer solution was sprayed onto each side of the PTFE sheet separately, the membrane thickness was easily controlled by the ionomer solution amount, and the deposition time and spray-travel path were carefully checked to secure repeatability and uniformity during the fabrication process. After fabricating the thin P/N RCM, the additional GO layer incorporation procedure was conducted (Figure 1d). The highly dispersed GO solution was selectively applied to the anode side of P/N RCM by forming an ultrathin-stacked structure. The layer comprising 2D GO nanosheets can act as a barrier to reactant gas (H_2 and O_2) crossover through the membrane. When the proton passes through the gap between the GO nanosheets, proton transfer via the vehicle mechanism can be improved due to the high water retention capacity of hydrophilic GO nanosheets.[34] After constructing P/N RCM-UG, to construct MEA, a Pt/C catalyst was deposited to both sides of the membrane using the same spraying deposition method (Figure 1e). The digital camera images of the fabricated P/N RCM-UG (left) and constructed MEA (right) are shown in Figure 1f.

2.2. Optimization of Spraying Conditions for P/N RCM

When the ionomer solution was sprayed from the spray nozzle and moved to the PTFE sheet, some parts of the volatile solvents (mainly IPA in this study) evaporated. The residue IPA solvent with low surface tension readily wetted the hydrophobic PTFE sheet, facilitating effective ionomer impregnation inside the porous PTFE sheet via capillary injection. To confirm the impact of IPA content on the impregnation of the PTFE sheet with ionomer, we compared two different concentrations of Nafion ionomer solution: 1 and 5 wt.%. The 5 wt.% Nafion ionomer solution exhibited inadequate impregnation properties, resulting in high opaqueness and the presence of solidified Nafion agglomerated particles on the membrane, even under the same fabrication process. In comparison, the 1 wt.% Nafion ionomer solution did not exhibit these issues. In the spray process, determining the proper discharged volume of ionomer solution from the nozzle (i.e., flow rate) is important to secure the proper residue solvent amount when reaching the PTFE sheet. In this study, three different flow rate conditions ($Q_{opt}/3$, Q_{opt}, and $3Q_{opt}$, where Q_{opt} = 0.22 mL min^{-1}) were investigated (**Figure 2**a–f). When the solution is sprayed from the spray nozzle, it exists in the form of a cluster, and the droplet size gradually becomes smaller as it is atomized while flying toward the substrate.[35] If the flow rate of the solution is low ($Q_{opt}/3$), most of the solvent evaporates during droplet flight. Therefore, the solidified ionomer particles can be deposited on the PTFE sheet as a marked yellow dotted circle in the scanning electron microscope (SEM) image (Figure 2a), while most porous PTFE sheets are unfilled with an ionomer. This effect allows the membrane to have opaque characteristics due to diffuse reflection in the void (i.e., filled with air) spaces inside the PTFE sheet (Figure 2d). Unlike low flow rates, under high flow rate conditions ($3Q_{opt}$), a large number of droplets are continuously ejected from the nozzle. Therefore, much residue solvent exists on the PTFE surface, and the following ionomer solution can collide with unsolidified ionomer clusters, resulting in flooding. As flooding occurs on the PTFE sheet surface, the previously deposited unsolidified ionomer clusters tend to spread outward and form large-ring-shaped structures by solidification. As a result, the membrane surface morphology exhibits a corrugated pattern wherein the ionomer-unfilled region coexists with the over-deposited region (Figure 2c,f). Under optimum flow rate conditions (Q), the proper amount of residue solvent helps the ionomer to be impregnated inside the PTFE sheet and can be evaporated and solidified before approaching the following ionomer solution. Therefore, the high quality of P/N RCM in terms of ionomer impregnation, symmetricity, and surface uniformity can be achieved by optimizing the flow rate condition. As shown in Figure 2b,e, P/N RCM has high transmittance and uniform thickness.

To analyze the optimal flow rate conditions for constructing P/N RCM through the spraying method, we introduced a simple theoretical model and suggested a "k" value as follows:

$$k = \frac{\textit{Covered Area by Droplets}}{\textit{Spray Spot Area}} = \frac{n\left(\frac{\pi}{4}D_0^2\right)}{\frac{\pi}{4}D_s^2} = n\left(\frac{D_0}{D_s}\right)^2 \quad (1)$$

where D_O is droplet diameters that sprayed out from the nozzle and D_s is spray-spot area on the substrate, respectively, and n represents the number of droplets. Notably, k = 1 means that the sprayed spot area would be completely covered with the impacted droplet ionomer solution without an overlapped region. For simplicity, we assumed that all the droplets were spared out from the nozzle with a uniform diameter of D_O. The spraying droplet size was assumed to be the same as the droplet deposited on the substrate, and it was estimated by averaging the deposited droplet size of the ionomer solution (Figure S4, Supporting Information). From the assumption, n can be calculated by introducing the terms of the total volume of sprayed droplets (U), flow rate (Q), spray-nozzle moving speed (V_n), and spraying duration time (τ) on a unit spot area.

$$n = \frac{Q\cdot\tau}{\frac{1}{6}\pi D_0^3} \text{ from the relation of } U = Q\cdot\tau = n\frac{1}{6}\pi D_0^3 \quad (2)$$

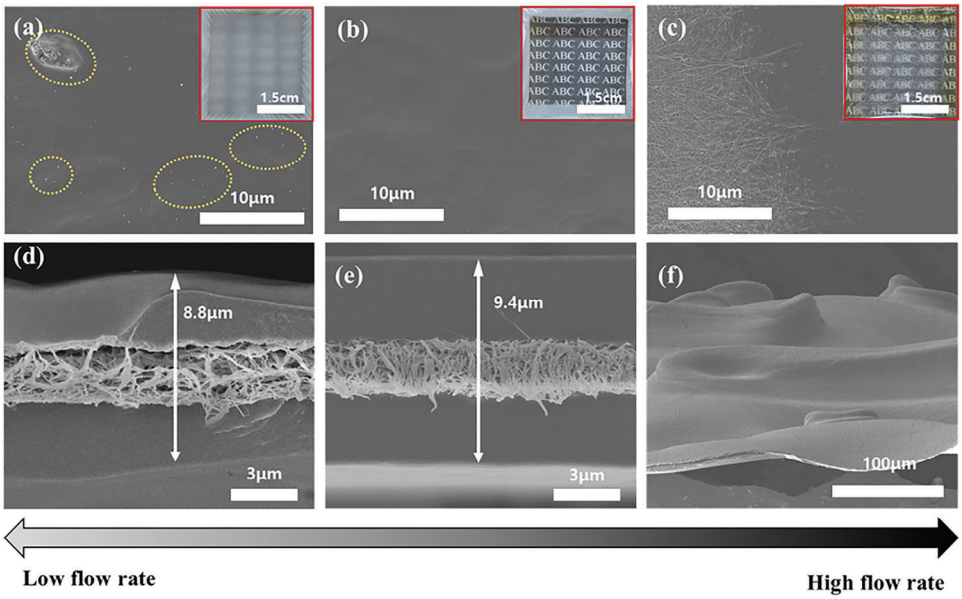

Figure 2. (a–f) SEM images of P/N RCM by varying the flow rate conditions of a) $Q_{opt}/3$, b) Q_{opt}, c) $3Q_{opt}$, where Q_{opt} = 0.22 mL min^{-1} and d–f) corresponding cross-sectional SEM images, respectively.

where Q is the three different flow rates used in experiments and τ is equal to D_s/V_n. Therefore, the "k" value can be represented as a function of Q, V_n, D_0, and D_s, in which key parameters are summarized in Table S1 (Supporting Information).

$$k = n\left(\frac{D_0}{D_s}\right)^2 = \frac{Q\cdot\tau}{\frac{1}{6}\pi D_0^3}\left(\frac{D_0}{D_s}\right)^2 = \frac{6Q}{\pi D_0^3}\frac{D_s}{V_n}\left(\frac{D_0}{D_s}\right)^2 = \frac{6Q}{\pi V_n D_0 D_s} \quad (3)$$

The values of "k" for different flow rates are plotted in **Figure 3**, where the k values for flow rates of Q/3, Q, and 3Q are calculated to be 0.59, 1.26, and 2.0, respectively. Notably, when the solution was applied at a flow rate of Q, the resulting k value was closest to the ideal value of 1, and this result agrees well with the observation of the well-impregnated P/N RCM with high transparency. For low Q values, liquid droplets failed to sufficiently cover the complete spot area with solidified ionomer particles from rapid solvent evaporation; however, excessive coverage of the liquid droplet-induced flooding would appear on the PTFE sheet surface for 3Q values. This finding suggests that optimizing spraying conditions such as flow rates by balancing the spray-spot area and number of droplets that covered the spot area is crucial for achieving highly impregnated and uniform P/N RCM. In this study, we identified the optimal spraying condition "Q" for constructing P/N RCMs and utilized this condition for incorporating an ultrathin GO layer and catalyst layers.

2.3. Characterization of GO

The SEM and TEM (transmission electron microscope) images (**Figure 4**a,b) show the anisotropic and elongated acicular grains of GO powders with wrinkled structures on the surface. A selected area electron diffraction (SAED) pattern of the GO

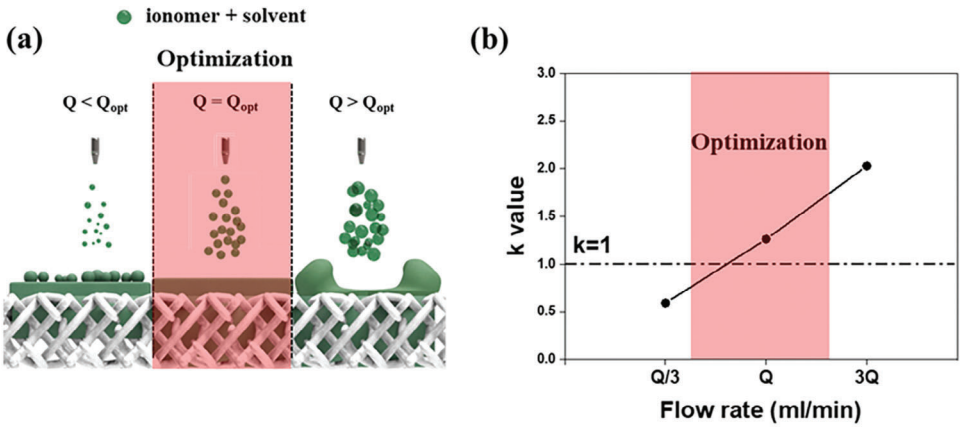

Figure 3. a) Schematics of the varying the flow rate conditions. b) Coverage indicator "k" for different flow rate conditions for P/N RCM construction.

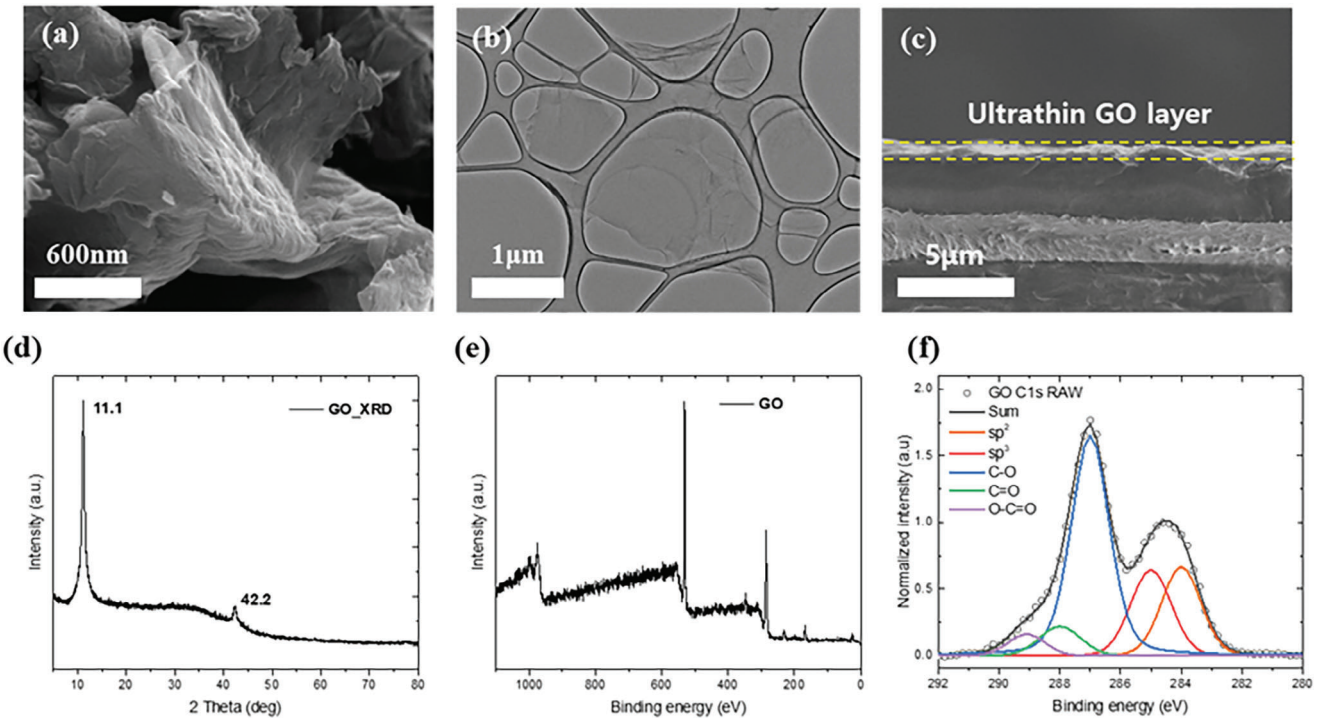

Figure 4. Morphological characterization of GO powders with a) SEM and b) TEM images, respectively. c) Cross-sectional SEM images of P/N RCM with an ultrathin GO layer. d) Structural characterizations of GO powders with XRD patterns, e) XPS full spectrum, and f) C 1s XPS spectra.

powders displayed several hexagonal rings with different spot sizes and the presence of domain boundaries in the selected regions, which confirmed that the GO powders comprised a multilayered structure of highly crystalline GO sheets (Figure S5, Supporting Information). The XRD (X-Ray diffraction) pattern (Figure 4d) indicates a sharp peak at 11.1 degrees, corresponding to the (001) lattice with spacing d_{001} ≈7.968 Å, and a small peak at 42.2 degrees, corresponding (101) lattices of in-plane graphitic sp^2 crystals with spacing d_{101} ≈2.141 Å.[36] The spacings of the samples were calculated using Bragg's law with a wavelength of 1.5412 Å.[36,37] The chemical structure of GO powder was analyzed using XPS (X-ray photoelectron spectroscopy) spectra (Figure 4e), revealing that the GO powder contained C, O, and S elements with a low C/O ratio of 1.38 compared to the general range of 1.5–2.5.[38] Figure 4f shows the C 1s XPS spectra of the GO powder normalized to the peak at 284.6 eV, and the spectra were deconvoluted into sp^2 (284 eV), sp^3 (284.6 eV), epoxy/hydroxyls (C—O, 286.6 eV), carbonyl (C═O, 288 eV), and carboxylates (O—C═O, 289.2 eV) bonds to calculate the proportion of chemical bonds. The GO shows a relatively low carbon amount of 38.71, including sp^2 and sp^3 peaks, which means that the GO used in this study has a high oxidation degree. Therefore, the dispersion characteristics of GO for constructing the ultrathin-stacked layer, as well as the water retention capacity for alleviating proton transport loss due to the insertion of non-ion-conducting materials, can be improved. The calculated values from the XPS spectra are summarized in Table S2 (Supporting Information). To compensate for the gas barrier property of thin P/N RCM (≈10 μm), an additional GO layer was introduced at the anode side of the membrane at the end of the membrane fabrication process under the same spraying conditions. The magnified inset image of the constructed membrane, as displayed in Figure 4c, showed the existence of an ultrathin GO-stacked layer (≈150 nm with GO loading amount of 0.011 mg cm^{-2}) at the outermost part of the membrane. In the case of the relatively lower loading amount of GO as 0.0056 mg cm^{-2}, it hardly acts as a gas barrier due to insufficient stacked layers of GO with ≈50 nm. The hydrogen crossover current density (HCCD) was reduced by 14.1%, while the GO with 150 nm showed a reduction of 46.9%. By considering a similar performance decay of 5% and 7.4% for 50 and 150 nm GO layers, respectively, the proper thickness of GO was determined as 150 nm (Figure S6, Supporting Information).

2.4. Characterizations of P/N RCM with Different GO Usages

Conventional methods of incorporating inorganic/organic fillers as reinforcing agents in the membrane involve simple mixing and dispersion of the fillers in the ionomer solution, followed by casting together. This results in random filler distribution within the membrane, often leading to agglomeration due to bulk evaporation during the membrane fabrication process. However, the spraying method is effective in controlling the spatial distribution of fillers due to layer-by-layer deposition characteristics. To confirm the efficacy of the GO-stacked layer on the membrane's outermost surface, a comparison of the GO spatial arrangement of GO in P/N RCM with layered and dispersed forms was further investigated (**Figure 5**a). Although the same loading GO amount of 0.011 mg cm^{-2} was used, the MEA with P/N RCMUG showed

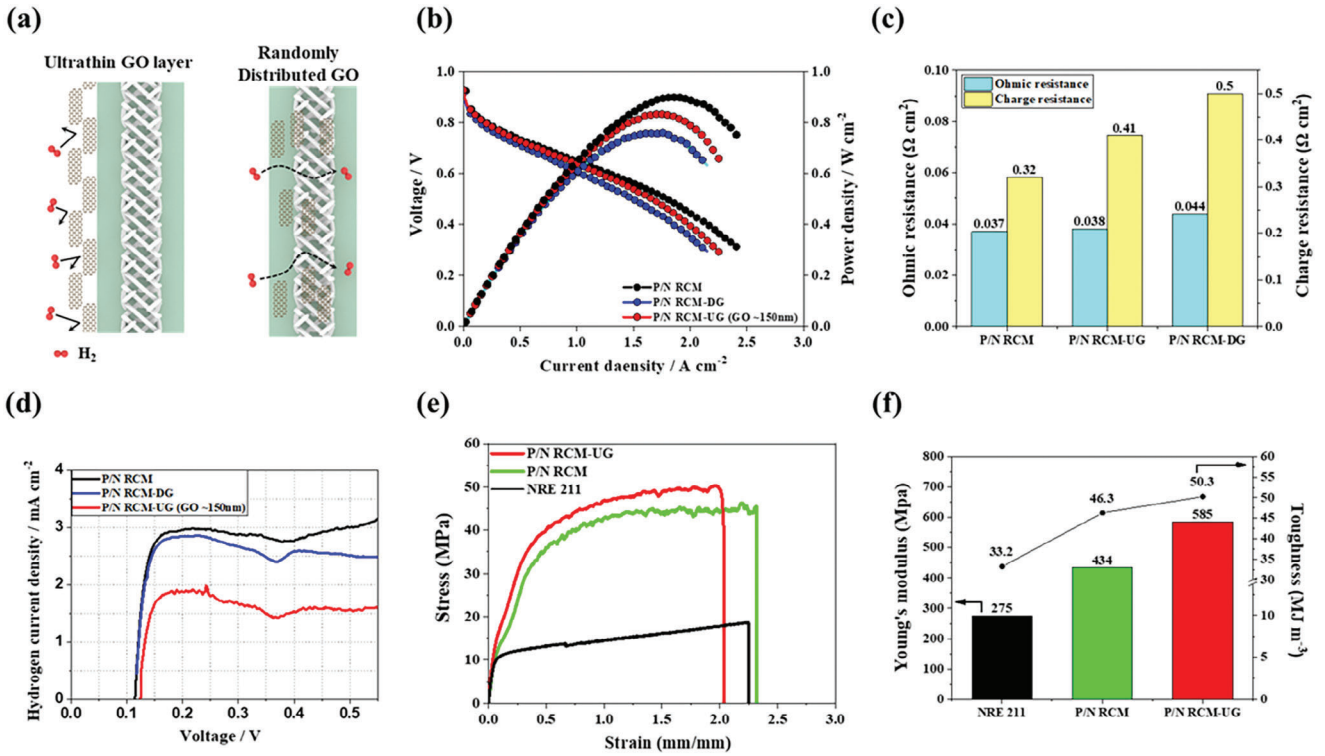

Figure 5. a) Schemes for the ultrathin GO layer and randomly distributed GO in P/N RCM. b) Polarization curves for the prepared three P/N RCMs with different GO distributions. c) Ohmic and charge transport resistances from EIS spectra at 0.8 V. d) LSV spectra for hydrogen crossover current densities. e) Stress–strain curves. f) Calculated values of Young's modulus and toughness.

a 9% higher performance (0.834 W cm^{-2}) than that of the P/N RCM with randomly distributed GO (P/N RCM-DG) (Figure 5b), with significantly smaller ohmic resistance (R_{ohm}) and charge resistance (R_{ct}) of 15.8% and 22%, respectively (Figure 5c) obtained from EIS (Electrochemical impedance spectroscopy) spectra at 0.8 V. Notably, the HCCD of the P/N RCM-UG was measured at 1.56 mA cm^{-2}, which is ≈62% lower than the P/N RCM-DG (Figure 5d). The following reasons explain the observed poor performance of the P/N RCM-DG. The spatially distributed GO cannot effectively block the gas crossover, and GO can clog the PTFE sheet pores to prevent ionomer impregnation into the sheet. In addition, the ultrathin GO layer at the membrane's outermost surface can prevent the clogging-induced reduction of Rohm while effectively reducing the reactant gas crossover, which notably increases as the membrane thickness decreases. Therefore, thin P/N RCM with high performance and high gas tightness can be synthesized using a GO layer. To further demonstrate the efficacy of the GO layer, electrochemical measurements for the MEA with a thicker P/N RCM membrane with 15 μm thickness have been conducted. As shown in Figure S7 (Supporting Information), the P/N RCM-UG with a 10 μm thickness exhibited a 20% lower hydrogen crossover current density than thicker P/N RCM with a 15 μm thickness, with only 2.6% reduction in maximum power density. The results indicate that the ultrathin GO layer can effectively block hydrogen crossover while minimizing performance sacrifice. The mechanical properties of P/N RCM-UG were investigated after confirming the efficacy of the GO-stacked layer for a gas barrier with minimal performance loss.

Figure 5e shows the stress–strain behavior of the prepared membranes of NRE 211 (commercial Nafion membrane with ≈26 μm thickness), P/N RCM, and P/N RCM-UG. Figure 5f shows the obtained key mechanical property indicators of Young's modulus and toughness. Young's modulus is the slope of the linear part of the stress–strain curve, and toughness is the ability of a material to absorb energy and plastically deform without fracturing, which can be calculated by integrating the stress–strain curve.[39,40] P/N RCM-UG exhibited the highest Young's modulus of 585 MPa and toughness of 50.3 MJ m^{-3} among the samples due to the reinforcing effect of mechanically robust PTFE sheet and further introduction of GO-stacked layers. Previous research has demonstrated that incorporating GO into the Nafion membrane can enhance the mechanical strength of the membrane.[41–44] This is because GO has a high Young's modulus of 200–600 GPa.[37,45–48] In the case of a layered structure, the effective Young's modulus can be calculated as the sum of the Young's modulus of each material in the layers multiplied by the respective thickness fraction.[49] Remarkably, even if the stiff layer is considerably thinner than the soft layer, a substantial enhancement in the effective Young's modulus is achievable. Although, in our experiment, GO flakes were sprayed and stacked to form a film, which results in a lower value than the intrinsic modulus of GO, their effective Young's modulus can still be much higher than the Nafion membrane. The measured Young's modulus of P/N RCM-UG, 585 MPa, can be calculated by considering the Young's modulus of approximately 10 GPa for the stacked GO layer. This result indicates that although the thickness fraction of

Table 1. Ion conductivity, dimensional stability, and water uptake of the prepared membranes..

Samples	Proton conductivity at 70 °C [S cm^{-1}]	Dimensional stability [length] [%]	Dimensional stability [thickness] [%]	Water uptake [%]
NRE 211	0.2126	19.2	16	26.2
P/N RCM	0.1856	5.6	27.2	20
P/N RCM-UG	0.1791	5.9	29.4	21.7

the GO layer in the membrane is only 1.5%, a 35% improvement in Young's modulus can be achievable. This mechanical property is further confirmed by the high dimensional stability of the membrane through the in-plane direction while higher changes in the thickness direction (**Table 1**), which means that the membrane can effectively resist mechanical failure even with a thin film thickness of ≈10 µm, with this thin film thickness compensating for the inevitable reduction of proton conductivity due to non-conducting materials.

2.5. Single-Cell Tests

To evaluate the performance and durability of the MEA with P/N RCM-UG, OCV wet/dry tests were conducted for the membrane and reference commercial NRE 211 membrane. The OCV wet/dry test based on the US DOE (Department of Energy) protocol was used for evaluating both the mechanical and chemical durability of MEAs.[50] The experimental protocol was operated at a constant temperature of 90 °C while repetitively changing the relative humidity (RH) between RH 100 to RH 0; this condition induced the mechanical failure of the membrane by repetitive swelling/shrinkage and chemical degradation of the membrane by radical attack. Under the OCV conditions of high temperature and low humidity, a large amount of reactive O_2 gas migrates to the anode side, and H_2 gas on the anode side crossover to the cathode side. And a direct chemical combustion reaction between H_2 and O_2 yields H_2O_2. The Fenton reaction of H_2O_2 and metal cations such as Fe^{2+} from the system generates hydroxyl (HO•) and hydroperoxyl (HOO•) radicals.

Figure 6a shows the OCV fluctuation of the MEAs during the test. MEA with P/N RCM-UG exhibited a much slower decay trend than that of NRE 211. P/N RCM-UG exhibited a lower OCV drop rate of 1.57 mV h^{-1} compared to that of NRE-211 of 3.17 mV h^{-1}, which is over 100% higher than that of P/N RCM-UG. This indicates that NRE 211 is chemically and mechanically mal-functioned, and P/N RCM-UG can impart high chemical and mechanical durability to MEA. This is due to the use of a porous PTFE sheet and the introduction of a gas barrier for alleviating radical generation. Figure 6b shows the polarization curves of the prepared MEAs before the OCV wet/dry test (i.e., BOL). The maximum power density (P_{max}) of the MEA with P/N RCM-UG (0.834 W cm^{-2}) exceeded that of the MEA with NRE 211 (0.779 W cm^{-2}) because the well-impregnated ionomer into the porous PTFE sheet under optimized spraying conditions alleviated proton transport loss due to the existence of the PTFE sheet, with the ultrathin GO layer imparting thinness to the membrane. Figure 6c shows the polarization curves

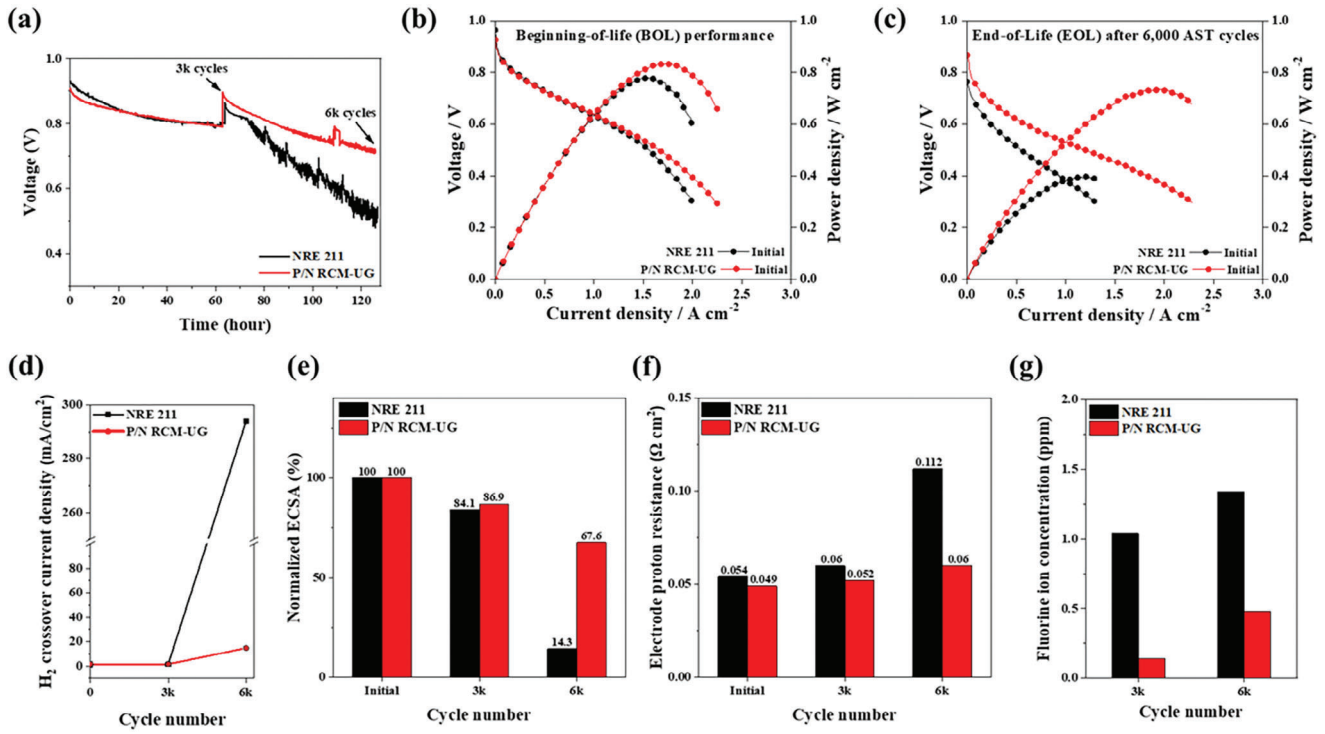

Figure 6. a) OCV spectra during an accelerated OCV wet/dry test for 125 h (6000 cycles). b,c) Polarization curves before (b) and after (c) OCV wet/dry test. d–g) Measured hydrogen crossover current density (d), normalized ECSA (e), electrode proton transport resistance (f), and fluoride ion concentration (g) after 0, 3000, and 6000 wet/dry cycles.

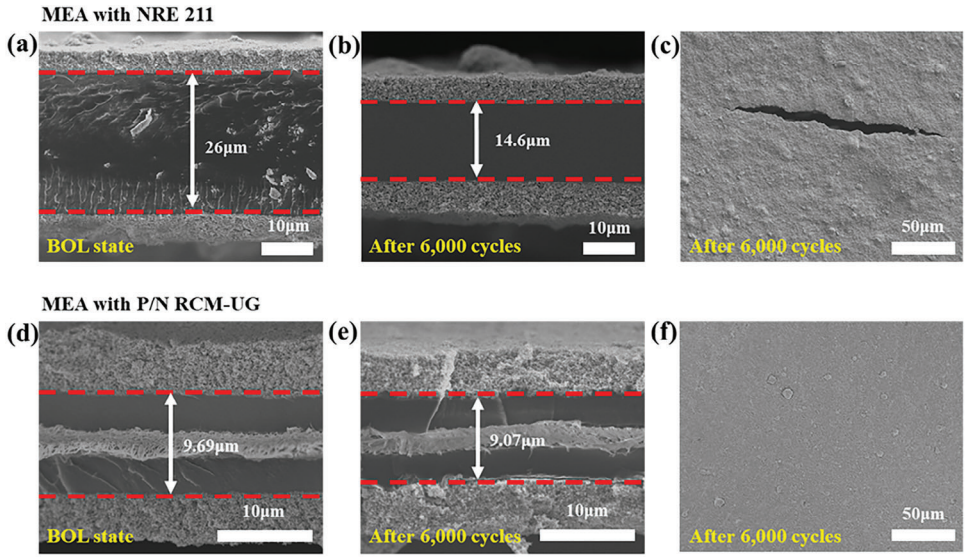

Figure 7. a–f) Cross-sectional and surface SEM images of MEAs with NRE 211 and P/N RCM-UG before and after OCV wet/dry cycles.

of MEAs after OCV wet/dry tests for 6000 cycles (corresponding to ≈125 h). The MEAs with NRE 211 exhibited a significantly reduced performance in all the current density regions, suggesting that the catalyst (i.e., activation loss), membrane (i.e., ohmic loss), and electrode degradation (i.e., overall loss, including electrode proton transport loss) occurred during the test, and showed a much lower P_{max} (0.395 W cm^{-2}) than the P/N RCM-UG (0.738 W cm^{-2}). Figure 6d displays the change in HCCD during the OCV wet/dry test at the initial state, after 3000, and 6000 cycles. As observed in the OCV fluctuation spectra, the MEA with NRE 211 was rapidly degraded after 3000 cycles and exhibited a significantly increased HCCD of 294 mA cm^{-2}, while the P/N RCM-UG showed 14.8 mA cm^{-2}, indicating that the NRE 211 mechanical degradation increased reactive gas crossover through the membrane, thereby accelerating radical generation and attack. Figure S9 (Supporting Information) shows the CV spectra during the wet/dry test at an initial state, after 3000, and 6000 cycles. For the MEA with NRE 211, the CV curve gradually rose in the + y direction (i.e., positive current) due to the oxidation reaction of H_2 near the cathode, which was attributed to increased gas crossover during the test. The electrochemically active surface area (ECSA) was also reduced by 85.7% in NRE 211 after 6000 cycles, while P/N RCM-UG dropped by 32.4% (Figure 6e). The decreased ECSA resulted from the decreasing triple-phase boundary due to the radical attack-induced degradation of the ionomer and catalyst. Figure 6f shows the electrode proton transport resistance calculated from the H_2/N_2 EIS spectra at 0.2 V based on the transmission line model. Figure S10 (Supporting Information) shows the EIS spectra for the MEAs with NRE 211 and P/N RCM-UG. The MEA with NRE 211 exhibited significantly increased proton transport resistance from 0.0368 Ω cm^2 (initial) to 0.1511 Ω cm^2 (6000 cycles), while the MEA with P/N RCM-UG exhibited a slight increase value from 0.0411 Ω cm^2 to only 0.0555 Ω cm^2. The rapid increase in electrode proton transport resistance may come from the interfacial contact issue between the membrane and electrode during wet/dry cycling as well as ionomer degradation from radical attack. To quantify the degree of chemical degradation of the membrane and ionomer with the same molecular structure as perfluorosulfonic acid that contains fluorine, the drain water during the OCV wet/dry test was collected after 3000 and 6000 cycles. The accumulated concentration of fluoride ions from drain water for 3000 (6000 cycles) was calculated as 1.2 ppm (1.5 ppm) and 0.126 ppm (0.478 ppm) for NRE 211 and P/N RCM-UG, respectively (Figure 6g).

As determined by post-mortem analysis of MEAs using SEM measurements, severe membrane thickness reduction of the MEA with NRE 211 (26–14.6 μm) in **Figure 7**a,b and electrode crack formation were observed during the OCV wet/dry test in Figure 7c. The reduction of membrane thickness is mainly attributed to chemical degradation induced by radical attack on the electrolyte membrane.[16,51–53] The generation of cracks in the electrode layer can be attributed to the greater dimensional change of NRE 211 in response to repetitive swelling/shrinking cycles of the electrode. However, the MEA with P/N RCM-UG exhibited almost similar membrane and electrode status compared to that of the initial state in Figure 7d–f. Therefore, using an optimized spraying method for impregnating ionomer into a PTFE sheet and the ultrathin gas barrier with a GO-stacked layer can impart thin film thickness to the membrane for high performance and durability against mechanical and chemical degradation due to high dimensional stability and alleviation of radical generation. The measured electrochemical properties of the prepared MEAs during OCV wet/dry test are summarized in **Table 2**.

3. Conclusion

This study demonstrated a spraying method for P/N RCM construction. The flow rate of the ionomer solution for optimally impregnating the ionomer into the porous PTFE sheet was optimized experimentally and confirmed using a simple theoretical droplet-spreading model. To secure the gas-blocking property for the thin membrane, the ultrathin GO-stacked layer was introduced at the membrane's outermost surface using the same spraying method. The proper GO loading amount and spatial

Table 2. Summary of the measured electrochemical properties of the prepared MEAs during OCV wet/dry test..

Samples	OCV [V]	P max [W cm^{-2}]	Current density at 0.6 V [A cm^{-2}]	Rohm [Ω cm^2] at 0.8 V	RLF-HF [Ω cm^2] at 0.8 V	LSV [mA cm^{-2}] at 0.5 V	ECSA [$]m^2$ $g_{pt}{}^{-1}$]	Electrode proton resistance [Ω cm^2]
Initial								
NRE 211	0.96	0.78	1.16	0.0478	0.3715	1.32	49.17	0.0538
P/N RCM-UG	0.93	0.83	1.2	0.0384	0.4143	1.54	53.28	0.0489
OCV wet/dry 3k cycles								
NRE 211	0.895	0.55	0.43	0.0428	2.1700	1.58	38.84	0.0595
	(−7.2%)	(−30%)	(−62.8%)	(−10.5%)	(+484.1%)	(+19.7%)	(−21%)	(+10.6%)
P/N RCM-UG	0.9	0.78	0.85	0.0404	1.0286	1.61	46.32	0.0521
	(−3.2%)	(−6.5%)	(−29.2%)	(+5.2%)	(+148.3%)	(+4.5%)	(−13.1%)	(+6.5%)
OCV wet/dry 6k cycles								
NRE 211	0.76	0.40	0.24	0.0503	6.0674	294	6.61	0.1120
	(−20.9%)	(−49.3%)	(−79.1%)	(+5.2%)	(+1533.2%)	(22 172.7%)	(−86.6%)	(+108.2%)
P/N RCM-UG	0.87	0.74	0.59	0.0407	1.8889	14.8	36.03	0.0597
	(−6.5%)	(−11.5%)	(−50.8%)	(+6%)	(+355.9%)	(+861%)	(−32.4%)	(+22.1%)

arrangement were also investigated in terms of electrochemical and mechanical properties. The MEA with optimized P/N RCM-incorporated ultrathin GO layer exhibited higher initial performance compared to commercial NRE 211, thanks to its thin film thickness of ≈10 μm, a feature of well-impregnated ionomer into non-conducting PTFE sheet, and alleviated gas crossover. Furthermore, the MEA exhibited significantly higher mechanical and chemical durability during the accelerated OCV wet/dry test. While the PTFE sheet imparted high dimensional stability to the membrane to withstand the swelling/shrinking during repetitive wet/dry conditions, introducing a gas barrier helps alleviate the generation of radicals by reducing reactive gas crossover through the membrane. We believe that this methodological approach with spraying techniques, which is widely used in the industrial field, will pave the way for developing high-performance and mechanically/chemically durable membranes for diverse electrochemical energy conversion devices.

4. Experimental Section

Preparation of Materials: Porous PTFE sheet (gen4; Donaldson Tetratex), graphite powder (325 mesh, 45 μm; Sigma–Aldrich), 2-propanol (99.5%; Samchun Chemical Inc.), Nafion ionomer solution (5 wt.%; Sigma–Aldrich), ethanol (99.5%; Samchun Chemical Inc.), and deionized (DI) water were used to fabricate the reinforced composite membrane. A Nafion ionomer was diluted to 1 wt.% using 2-propanol, and GO powder was dispersed in ethanol and DI water with 0.02 wt.%. Sulfuric acid (70%; Samchun Chemical Inc.) was diluted with DI water to have a 1 M concentration and was used for membrane reprotonation. A Pt/C catalyst (46.9 wt.%; Tanaka Inc.) was used for MEA construction. A total ionic strength adjuster buffer solution and calibrated fluoride ion-selective electrode (A214, Thermo Scientific) were used to measure fluoride ion concentration.

Synthesis of GO: A graphite source (3 g) was mixed with a H_2SO_4/H_3PO_4 (360: 40 mL) solution. Then, a $KMnO_4$ oxidant was dropped into the mixture under vigorous stirring at 800 rpm for 10 min. The reaction continued for 22 h at 50 °C, and the neutralization process was followed by adding DI water (400 mL) and H_2O_2 (3 mL, 30%) at 1200 rpm in the ice bath. Afterward, a vacuum filtration process was performed, and multiple steps of rinsing with centrifugation at 4,000 rpm were conducted. The precipitated GO was refiltered to obtain a GO cake, and the dehydration process with a 48 h freezing dry was executed. Finally, the GO powder was obtained by grinding the GO cake in a bowl.

Fabrication of the Reinforced Composite Membrane and MEA: The diluted Nafion ionomer solution was sprayed onto a PTFE sheet using a lab-made spray-coating system. This system was constructed by combining an airbrush with a commercial 3D printing machine (Ender-3; Shenzhen). When we sprayed the Nafion ionomer solution, since the solution was more infiltrated into the porous PTFE sheet when sprayed initially, a 1.4 times larger ionomer solution was sprayed to the first front side than the after backside to ensure symmetrical placement of the porous PTFE sheet. After spraying the Nafion ionomer and GO solution, the fabricated membrane was dried at 80°C for 1 h to remove residual solvent and annealed at 130 °C for 2 h to improve Nafion crystallization. Following the annealing process, sulfuric acid treatment was performed at 80 °C for 1 h, and the residue solvent was thoroughly washed away with deionized water. Next, to fabricate MEA, a catalyst slurry comprising a Pt/C catalyst, Nafion ionomer, DI, and 2-propanol was prepared with an ionomer-to-carbon ratio of 0.6. The dispersion process for the catalyst slurry was performed using a vortex mixer and ultrasonication treatment. Then, the prepared catalyst slurry was deposited onto the fabricated membrane using the same spraying method. All the MEAs were manufactured with the same catalyst loading amount of 0.2 mg_{Pt} cm^{-2} for both the anode and cathode, with an active area of 5 cm^2.

Characterization: Surface and cross-sectional images of the membranes were measured using an FE-SEM (JSM-7410F; JEOL LTD) at a 5 kV accelerating voltage. To measure ion conductivity, samples were cut into 1 × 4 cm sizes and placed in contact with four Pt wires spaced 1 cm apart, and the assembly was tightly fastened using two-end plates and 8 bolts. The EIS was performed with the 4-point method by supplying fully humidified N_2 gas at 70 °C, after which the in-plane ion conductivity (σ) was calculated using Equation 4:

$$\sigma = \frac{L}{R \times A} \quad (4)$$

where L, R, and A represent the width, resistance, and thickness of the membrane, respectively. The water uptake capacity and dimensional stability of the membranes were calculated using the following equations:

$$\text{Thickness change } (\%) = 100 \times \frac{\Delta t}{t_i} \quad (5)$$

$$\textit{Length change } (\%) = 100 \times \frac{\Delta L}{L_i} \quad (6)$$

$$\textit{Water uptake } (\%) = 100 \times \frac{\Delta m}{m_i} \quad (7)$$

To obtain the initial thickness (t_i), length (L_i), and mass (m_i) of the membrane, the membrane was cut into 1 × 1 cm size and dried in a vacuum oven at 80 °C for 12. After cooling to room temperature, each value of t_i, L_i, and m_i was measured. The final thickness (t_f), length (L_f), and mass (m_f) were obtained by fully hydrating the membranes with DI water at 80 °C for 12 h and removing residual water on the membrane surface. The Δ value was calculated as the final value minus the initial value.

Single-Cell Test and OCV Wet/Dry Durability Test: The single cell was constructed by assembling each fuel cell part of the gas diffusion layers (39BB), Teflon gaskets, bipolar plates (Graphite, 1 mm channel height and width), and the prepared MEA. After connecting the single cell to the PEMFC station (CNL Energy Inc.), the polarization curves were obtained using the current sweep method at a scan rate of 50 mA cm^{-2} under cell temperatures of 80 °C and RH100 by supplying fully humidified H_2 (300 mL min^{-1}) and air (1000 mL min^{-1}) to the anode and cathode, respectively. Under the same conditions, the corresponding EIS spectra were obtained using an impedance analyzer (HCP-803; BioLogic Inc.) with an amplitude of 10 mV and a frequency range of 100 kHz–100 mHz at 0.8 V. To calculate the ECSAs, CV spectra were measured using a potentiostat (HCP-803; BioLogic Inc.) at a scan speed of 100 mV s^{-1} under 0.05–1.2 V by supplying fully humidified H_2 (50 mL min^{-1}) and N_2 (200 mL min^{-1}) to the anode (pseudo reference and counter electrode) and cathode (working electrode), respectively. After changing the H_2 flow rate to 200 mL min^{-1}, LSV was measured at a scan speed of 2 mV s^{-1} under 0.1 – 0.55 V. The HCCD was determined at 0.5 V. Under the same conditions, H_2/N_2 EIS was conducted to analyze the electrode proton transport resistance at 0.2 V, with an AC amplitude of 5 mV and a frequency of 70 mHz–100 kHz.[54] After completing the initial performance test of MEA, an OCV wet/dry test was conducted. For this experiment, fully humidified H_2 and air gas were applied at 200 mL min^{-1} every 45 s, followed by non-humidified H_2 and air gas applied at 200 mL min^{-1} every 30 s at a cell temperature of 90 °C, and this constitutes 1 cycle. During the repeated cycling test, the IV curve, EIS spectra, CV spectra, and LSV were measured at 3000 and 6000 cycles. Drain water was collected at 3000 and 6000 cycles to examine the concentration of emitted fluorine ions.

Supporting Information

Supporting Information is available from the Wiley Online Library or from the author.

Acknowledgements

E.H.C and H.J.K contributed equally to this work. J.H.K and H.S.A from AHN Materials Inc. provide the GO powders for this study. This work was supported by the Technology Innovation Program, grant number 20020437, funded by the Ministry of Trade, Industry and Energy (MOTIE, Korea) and the National Research Foundation of Korea (NRF), grant no. 2022R1F1A1064385 and RS-2023-00217661.

Conflict of Interest

The authors declare no conflict of interest.

Data Availability Statement

The data that support the findings of this study are available from the corresponding author upon reasonable request.

Keywords

durable fuel cells, gas barriers, graphene oxide, PTFE sheets, reinforced thin membranes

Received: July 18, 2023
Revised: October 28, 2023
Published online:

[1] S. J. Hamrock, M. A. Yandrasits, *J. Macromol. Sci. Part C* **2006**, *46*, 219.
[2] J. Wu, X. Z. Yuan, J. J. Martin, H. Wang, J. Zhang, J. Shen, S. Wu, W. Merida, *J. Power Sources* **2008**, *184*, 104.
[3] R. Borup, J. Meyers, B. Pivovar, Y. S. Kim, R. Mukundan, N. Garland, D. Myers, M. Wilson, F. Garzon, D. Wood, P. Zelenay, K. More, K. Stroh, T. Zawodzinski, J. Boncella, J. E. Mcgrath, M. Inaba, K. Miyatake, M. Hori, K. Ota, Z. Ogumi, S. Miyata, A. Nishikata, Z. Siroma, Y. Uchimoto, K. Yasuda, K.-I. Kimijima, N. Iwashita, *Chem. Rev.* **2007**, *107*, 3904.
[4] S. Zhang, X. Yuan, H. Wang, W. Merida, H. Zhu, J. Shen, S. Wu, J. Zhang, *Int. J. Hydrog. Energy* **2009**, *34*, 388.
[5] V. A. Sethuraman, J. W. Weidner, A. T. Haug, L. V. Protsailo, *J. Electrochem. Soc.* **2008**, *155*, B119.
[6] Y. Wang, K. S. Chen, J. Mishler, S. C. Cho, X. C. Adroher, *Appl. Energy* **2011**, *88*, 981.
[7] C. Bi, H. Zhang, S. Xiao, Y. Zhang, Z. Mai, X. Li, *J. Membr. Sci.* **2011**, *376*, 170.
[8] F. Liu, B. Yi, D. Xing, J. Yu, H. Zhang, *J. Membr. Sci.* **2003**, *212*, 213.
[9] G. Dorenbos, K. Morohoshi, *Energy Environ. Sci.* **2010**, *3*, 1326.
[10] J.-E. Cha, S. Jang, D.-J. Seo, J. Hwang, M. H. Seo, Y.-W. Choi, W. B. Kim, *Chem. Eng. J.* **2023**, *454*, 140091.
[11] S. Shi, A. Z. Weber, A. Kusoglu, *J. Membr. Sci.* **2016**, *516*, 123.
[12] W. Liu, T. Suzuki, H. Mao, T. Schmiedel, *ECS Trans.* **2013**, *50*, 51.
[13] K. A. Lee, K. R. Yoon, S. H. Kwon, K. J. Lee, S. Jo, J. S. Lee, K.-Y. Lee, S. W. Lee, S. G. Lee, J. Y. Kim, *J. Mater. Chem. A* **2019**, *7*, 7380.
[14] S. Lim, J.-S. Park, *Energies* **2020**, *13*, 6101.
[15] N. Il Kim, B. G. Seo, H. W. Park, J. W. Shim, H. J. Kong, J. H. Shim, *J. Membr. Sci.* **2023**, *679*, 121668.
[16] B. Wu, M. Zhao, W. Shi, W. Liu, J. Liu, D. Xing, Y. Yao, Z. Hou, P. Ming, J. Gu, Z. Zou, *Int. J. Hydrog. Energy* **2014**, *39*, 14381.
[17] M. Inaba, T. Kinumoto, M. Kiriake, R. Umebayashi, A. Tasaka, Z. Ogumi, *Electrochim. Acta* **2006**, *51*, 5746.
[18] M. Chen, C. Zhao, F. Sun, J. Fan, H. Li, H. Wang, *eTransportation* **2020**, *5*, 100075.
[19] M. Han, Y.-G. Shul, H. Lee, D. Shin, B. Bae, *Int. J. Hydrog. Energy* **2017**, *42*, 30787.
[20] X. Luo, L. Ghassemzadeh, S. Holdcroft, *Int. J. Hydrog. Energy* **2015**, *40*, 16714.
[21] A. M. Baker, L. Wang, W. B. Johnson, A. K. Prasad, S. G. Advani, *J. Phys. Chem.* **2014**, *118*, 26796.
[22] B. P. Pearman, N. Mohajeri, R. P. Brooker, M. P. Rodgers, D. K. Slattery, M. D. Hampton, D. A. Cullen, S. Seal, *J. Power Sources* **2013**, *225*, 75.
[23] J. Choi, J. H. Yeon, S. H. Yook, S. Shin, J. Y. Kim, M. Choi, S. Jang, *ACS Appl. Mater. Interfaces* **2021**, *13*, 806.
[24] K. R. Yoon, K. A. Lee, S. Jo, S. H. Yook, K. Y. Lee, I.-D. Kim, J. Y. Kim, *Adv. Funct. Mater.* **2019**, *29*, 1806929.

[25] A. M. Baker, S. M. Stewart, K. P. Ramaiyan, D. Banham, S. Ye, F. Garzon, R. Mukundan, R. L. Borup, *J. Electrochem. Soc.* **2021**, *168*, 024507.
[26] E. Endoh, *ECS Trans.* **2008**, *16*, 1229.
[27] A. M. Baker, D. Torraco, E. J. Judge, D. Spernjak, R. Mukundan, R. L. Borup, S. G. Advani, A. K. Prasad, *ECS Trans.* **2015**, *69*, 1009.
[28] A. M. Baker, J. H. Dumont, R. Mukundan, S. G. Advani, A. K. Prasad, D. Spernjak, R. L. Borup, *ECS Trans.* **2017**, *80*, 643.
[29] H. Beydaghi, M. Javanbakht, E. Kowsari, *Ind. Eng. Chem. Res.* **2014**, *53*, 16621.
[30] T. Bayer, S. R. Bishop, M. Nishihara, K. Sasaki, S. M. Lyth, *J. Power Sources* **2014**, *272*, 239.
[31] R. R. Nair, H. A. Wu, P. N. Jayaram, I. V. Grigorieva, A. K. Geim, *Science* **2012**, *335*, 442.
[32] M. Breitwieser, T. Bayer, A. Büchler, R. Zengerle, S. M. Lyth, S. Thiele, *J. Power Sources* **2017**, *351*, 145.
[33] S. Lee, W. Jang, M. Kim, J. E. Shin, H. B. Park, N. Jung, D. Whang, *Small* **2019**, *15*, 1903705.
[34] R. P. Pandey, A. K. Thakur, V. K. Shahi, *ACS Appl. Mater. Interfaces* **2014**, *6*, 16993.
[35] H. Chen, X. Ding, X. Pan, T. Hayat, A. Alsaedi, Y. Ding, S. Dai, *J. Power Sources* **2018**, *402*, 82.
[36] J. H. Kim, G. H. Shim, T. T. N. Vo, B. Kweon, K. M. Kim, H. S. Ahn, *RSC Adv.* **2021**, *11*, 3645.
[37] L. Wang, J. Kang, J.-D. Nam, J. Suhr, A. K. Prasad, S. G. Advani, *ECS Electrochem. Lett.* **2015**, *4*, F1.
[38] R. Al-Gaashani, A. Najjar, Y. Zakaria, S. Mansour, M. A. Atieh, *Ceram. Int.* **2019**, *45*, 14439.
[39] A. Galeski, *Prog. Polym. Sci.* **2003**, *28*, 1643.
[40] S. J. Hong, H. Y. Jung, S. J. Yoon, K.-H. Oh, S.-G. Oh, Y. T. Hong, D. M. Yu, S. So, *J. Power Sources* **2022**, *551*, 232221.
[41] L. Liu, J. Zhang, J. Zhao, F. Liu, *Nanoscale* **2012**, *4*, 5910.
[42] Q. Peng, S. De, *RSC Adv.* **2013**, *3*, 24337.
[43] C. Gómez-Navarro, M. Burghard, K. Kern, *Nano Lett.* **2008**, *8*, 2045.
[44] P. Poulin, R. Jalili, W. Neri, F. Nallet, T. Divoux, A. Colin, S. H. Aboutalebi, G. Wallace, C. Zakri, *Proc. Natl. Acad. Sci. USA* **2016**, *113*, 11088.
[45] J. W. Suk, R. D. Piner, J. An, R. S. Ruoff, *ACS Nano* **2010**, *4*, 6557.
[46] S. Mondal, F. Papiya, S. N. Ash, P. P. Kundu, *J. Environ. Chem. Eng.* **2021**, *9*, 104945.
[47] D. C. Seo, I. Jeon, E. S. Jeong, J. Y. Jho, *Polymers* **2020**, *12*, 1375.
[48] R. Kumar, C. Xu, K. Scott, *RSC Adv.* **2012**, *2*, 8777.
[49] A. Upadhyay, R. Singh, *Mod. Mech. Eng.* **2012**, *02*, 6.
[50] U.S Department of Energy Fuel Cell Technologies, "Fuel cells multi-year research, development & demonstration plan.", https://www.energy.gov/sites/prod/files/2017/11/f46/FCTT_Roadmap_Nov_2017.pdf (accessed: 2023 April).
[51] S. Xiao, H. Zhang, C. Bi, Y. Zhang, Y. Zhang, H. Dai, Z. Mai, X. Li, *J. Power Sources* **2010**, *195*, 5305.
[52] L. Wang, S. G. Advani, A. K. Prasad, *Electrochim. Acta* **2013**, *109*, 775.
[53] M. Zhao, W. Shi, B. Wu, W. Liu, J. Liu, D. Xing, Y. Yao, Z. Hou, P. Ming, Z. Zou, *Electrochim. Acta* **2015**, *153*, 254.
[54] J. Choi, D. Kim, J. E. Chae, S. Lee, S. M. Kim, S. J. Yoo, H. J. Kim, M. Choi, S. Jang, *ACS Appl. Mater. Interfaces* **2022**, *14*, 50956.